Geoscientific
Model Development
Discussions
Open Access
EGU

Source apportionment of atmospheric water over East Asia – a source tracer study in CAM5.1

Chen Pan[1], Bin Zhu[1], Jinhui Gao[1], Hanqing Kang[1]

[1]Key Laboratory of Meteorological Disaster, Ministry of Education (KLME), Joint International Research Laboratory of Climate and Environment Change (ILCEC), Collaborative Innovation Center on Forecast and Evaluation of Meteorological Disasters, Key Laboratory for Aerosol-Cloud-Precipitation of China Meteorological Administration, Nanjing University of Information Science & Technology, Nanjing, 210044, China

Correspondence to: Bin Zhu (binzhu@nuist.edu.cn)

Geoscientific
Model Development
Discussions

9 **Abstract**

10 The atmospheric water tracer (AWT) method is implemented in the Community Atmosphere Model version 5.1 (CAM5.1)

11 to quantitatively identify the contributions of various source regions to precipitation and water vapour over East Asia.

12 Compared to other source apportionment methods, the AWT method was developed based on detailed physical

13 parameterizations, and can therefore trace the behaviour of atmospheric water substances directly and exactly. According to

14 the simulation, the north Indian Ocean (NIO) is the dominant oceanic moisture source region for precipitation over the

15 Yangtze River Valley (YRV) and South China (SCN) in summer, while the Northwest Pacific (NWP) dominates during

16 other seasons. Evaporation over the South China Sea (SCS) is responsible for only 2.8–4.2% of summer precipitation over

17 the YRV and SCN. In addition, the Indo-China Peninsula is an important terrestrial moisture source region (annual

18 contribution of ~10%). The overall relative contribution of each source region to the water vapour amount is similar to the

19 corresponding contribution to precipitation over the YRV and SCN. A case study for the SCS shows that only a small part

20 (≤5.8%) of water vapour originates from local evaporation, while much more water vapour is supplied by the NWP and NIO.

21 In addition, because evaporation from the SCS represents only a small contribution to the water vapour over the YRV and

22 SCN in summer, the SCS mainly acts as a water vapour transport pathway where moisture from the NIO and NWP meet.

23

24 **Keywords**

25 Atmospheric water tracer method; Community Atmosphere Model; source apportionment; precipitation and water vapour

1 Introduction

Water vapour is the most important component of the atmosphere, affecting global climate and weather patterns (Held and Soden, 2000). Among current studies of the hydrological cycle, the identification of moisture sources to the atmosphere is an important topic, because a better understanding of these sources will benefit long-term forecasting, disaster prevention and allocation of water resources (Bosilovich and Schubert, 2002).

Source apportionment methods have been developed to identify atmospheric moisture source regions. These methods generally can be divided into three types, namely analytical models, isotopes and numerical (Lagrangian and Eulerian) atmospheric water tracers (AWTs) (Gimeno et al., 2012). In addition, sensitivity experiments in numerical simulations such as shutting down water vapour flux at the lateral boundaries or surface evaporation (Chow et al., 2008) are an approach to study the contributions of moisture from diverse regions. Analytical models, widely used in earlier studies (Brubaker et al., 1993; Burde and Zangvil, 2001; Eltahir and Bras, 1996; Savenije, 1995; Trenberth, 1999), are generally based on various simplifying assumptions such as a well-mixed atmosphere. The stable isotopes of water, HDO and $H_2^{18}O$, can be used to investigate the water cycle. However, water isotope data reflect a series of processes that occur simultaneously, which makes it difficult to interpret isotope results for the water cycle (Numaguti, 1999; Sodemann and Zubler, 2010). The Lagrangian method has become a popular way to analyse the transport of moisture and moisture sources of precipitation (Dirmeyer and Brubaker, 1999; Gustafsson et al., 2010; Sodemann et al., 2008; Stohl and James, 2004; Stohl et al., 2008). However, Gimeno et al. (2012) pointed out that the treatments of water vapour transport and changes of atmospheric water vapour in the Lagrangian method are not based on detailed physical equations. Sodemann and Zubler (2010) pointed out that a strong bias exists in Lagrangian precipitation estimates, because all cloud processes are neglected. Sensitivity experiments generally contain nonlinearities, which may lead to changes in the dynamic and thermodynamic structures of meteorological fields, suggesting that their results cannot be used to directly diagnose moisture sources. In contrast, the Eulerian AWT method has been developed based on detailed physical parameterizations in atmospheric models, enabling a direct and exact tracking of the behaviour of atmospheric water substances (Numaguti, 1999; Bosilovich, 2002).

50

51   The Eulerian AWT method was firstly developed by Joussaume et al. (1986) and Koster et al. (1986) for global circulation

52   models (GCMs). Later, this AWT method was applied to diagnose regional water sources in GCMs. For example, Numaguti

53   (1999) identified the moisture sources of Eurasian precipitation, and Bosilovich and Schubert (2002) diagnosed the moisture

54   sources of precipitation over North America and India. Bosilovich et al. (2003) studied water sources of the large-scale

55   North American monsoon, Bosilovich (2002) investigated the vertical distribution of water vapour tracers over North

56   America and Sodemann et al. (2009) used this method to study sources of water vapour leading to a flood event in Central

57   Europe using a mesoscale model. Finally, Knoche and Kunstmann (2013) incorporated the AWT method into a fifth-

58   generation mesoscale model to study the transport of atmospheric moisture in West Africa.

59

60   In summer, the Asian summer monsoon (ASM) brings large amounts of water vapour to the East Asian (EA) continent,

61   leading to a wet season and abundant precipitation. Simmonds et al. (1999) pointed out that the dominant moisture transport

62   pathways during summer can be divided into three branches, namely (i) southwesterly flow associated with the Indian

63   summer monsoon, (ii) southerly or southeasterly flow associated with the southeastern Asian monsoon, and (iii) the mid-

64   latitude Westerlies. Correspondingly, these pathways transport moisture from (i) the Bay of Bengal (BOB) and the Arabian

65   Sea (AS), (ii) the South China Sea (SCS) and the Northwest Pacific (NWP) and (iii) the mid-latitude regions. Simmonds et al.

66   (1999) and Xu et al. (2008) pointed out that the BOB to SCS are the main source regions for rainfall over southeast China.

67   Using the Lagrangian Flexible Particle (FLEXPART) dispersion model (Stohl and James, 2004), Drumond et al. (2011)

68   discovered that the inland regions of China receive moisture mostly from western Asia, while the East China Sea (ECS) and

69   SCS are the main source regions for rainfall in China's eastern and southeastern coastal areas and the AS and BOB are the

70   main source regions for southern and central China from April to September. With the FLEXPART model, Baker et al.

71   (2015) demonstrated that the Indian Ocean is the primary source of moisture for East Asian summer monsoon (EASM)

72   rainfall. Using the same model, Chen et al. (2013) suggested that the ECS, the SCS, the Indian peninsula and BOB and the

73   AS were the four major moisture source regions for summer water vapour over the Yangtze River Valley (YRV) during

74   2004–2009. Chow et al. (2008) suggested that water vapour supplied by the Indian summer monsoon contributed about 50%

75 to early summer precipitation over China in 1998, and inferred that the SCS may act as a pathway for water vapour transport

76 affected by the Indian and Southeast Asian summer monsoon. However, recently Wei et al. (2012), using a Lagrangian

77 model, showed that the major moisture transport pathways to the YRV are over land and not over the ocean. Therefore, the

78 dominant source regions of moisture for summer rainfall over EA are still uncertain.

79

80 Baker et al. (2015) pointed out that the water vapour transport mechanisms for precipitation over China during the ASM are

81 still unquantified. Previous studies have pointed out that analytical models need simplifying assumptions, isotope data not

82 only reflect the water cycle, the Lagrangian methods lack cloud processes and that sensitivity experiments contain

83 nonlinearities, limiting diagnostic studies of moisture sources. On the other hand, the Eulerian AWT method does not have

84 these shortcomings and is an accurate way to quantitatively determine water sources (Bosilovich, 2002). Therefore, in this

85 study, we aim at incorporating an Eulerian AWT approach into an advanced global atmosphere model – the Community

86 Atmosphere Model version 5.1 (CAM5.1) (Neal et al., 2012). Using this method, we address the following questions: (1)

87 What moisture source regions are most important for precipitation and water vapour amount over EA, including the YRV

88 and South China (SCN)? (2) What is the role of the SCS for precipitation and water vapour amount over EA during the

89 EASM: a dominant source region or just a pathway for water vapour transport from other source regions?

90

91 In this study, detailed descriptions of physical parameterization schemes and means of implementing the AWT mechanisms

92 in CAM5.1 are given in Sect. 2. Simulation results, including evaluation and discussion, are presented in Sect. 3. Finally,

93 summary and concluding remarks are presented in Sect. 4.

94

95 **2 Model and methods**

96 The CAM5.1, released by the U.S. National Center for Atmospheric Research, is the atmospheric component of the

97 Community Earth System Model (CESM) (Neal et al., 2012). Compared to CAM4, CAM5.1 contains a range of

98 improvements in the representation of physical processes such as moist turbulence, shallow convection, stratiform

99   microphysics, cloud macrophysics schemes and others (Neal et al., 2012). The horizontal resolution used in this study is 1.9°

100 in latitude and 2.5° in longitude. The vertical range is from the surface to approximately 4 hPa ($\approx$ 40 km).

101

102 In this study, the chemistry mechanism of CAM5.1 is taken from MOZART-4 (Emmons et al., 2010), in which water vapour

103 is invariant, which means that it is unnecessary to consider changes in water vapour during chemical processes. The temporal

104 evolution of the mass mixing ratios (MMRs) of different water substances (water vapour, cloud droplets and ice) is

105 determined by deep convection, shallow convection, cloud macrophysics, cloud microphysics, advection and vertical

106 diffusion. To diagnose the dominant moisture source regions of atmospheric water over EA, the global surface is divided

107 into 25 source regions as shown in Fig. 1. Most regions are defined based on the locations of continents and oceans. Due to

108 the focus on moisture sources over EA in this study, EA and its adjacent regions are further divided to provide more detail.

109 Within source region k, the surface flux of the tagged water vapour tracer E^k is equal to the surface evaporation flux of

110 water vapour E; otherwise $E^k = 0$. As in the treatment described in Knoche and Kunstmann (2013) and Bosilovich and

111 Schubert (2002), water is "tagged" when it evaporates at its source region and is no longer tagged when it precipitates from

112 the atmosphere to the Earth's surface via atmospheric processes. When previously tagged precipitation reevaporates from the

113 surface, it is regarded as newly tagged water (Knoche and Kunstmann, 2013), which then belongs to the region from where it

114 reevaporates.

115

116 The MMRs of water vapour, cloud droplets and ice at a particular level are defined as q_v, q_l and q_i, respectively. The

117 corresponding MMRs of tagged water substances from source region k are $q_{v,tg}^k$, $q_{l,tg}^k$ and $q_{i,tg}^k$. All these tagged water

118 substances are passive, which means that they are entirely separate from the original water substances in CAM5.1 and have

119 no impact on dynamical and thermal fields. Numaguti (1999) suggested that the lifetime of atmospheric water vapour is

120 about 10 days. In this study, the simulation is started in 01 January 1997, and the initial MMRs of tagged substances are set

121 to zero. To attain stable initial concentrations of tagged water substances, the simulation experiment takes a year to spin up.

122 We then investigate the ten-year averaged results for 1998 to 2007. In the following, we describe the treatment of tagged

123 AWTs in CAM5.1's physical parameterizations.

124

2.1 Deep convection

126   In CAM5.1, deep convection is parameterized using the approach described in Zhang and McFarlane (1995), but with

127   modifications following Richter and Rasch (2008) and Raymond and Blyth (1986, 1992). In the calculation of consistent

128   transport of deep convection, we assume the ratio of tagged and original water vapour tendencies, respectively denoted as

129    $\left(\frac{\partial q_{v,tg}^k}{\partial t}\right)_{\mathrm{dp}}$ and $\left(\frac{\partial q_v}{\partial t}\right)_{\mathrm{dp}}$, is equal to the ratio of the relevant tagged water vapour MMR and the corresponding sum, expressed

130   as:

131    $$\left(\frac{\partial q_{v,tg}^k}{\partial t}\right)_{\mathrm{dp}} = \frac{q_{v,tg}^k}{\sum_{k=1}^n q_{v,tg}^k} \times \left(\frac{\partial q_v}{\partial t}\right)_{\mathrm{dp}} \tag{1}$$

132   In this study, n=25, which is the total number of defined source regions (Fig. 1). In this scheme, the assumed ratio

133   relationship in Eq. (1) is also used to calculate the production of tagged cloud water in updraft, as well as the tagged rain

134   production rate and evaporation rate of tagged rain in downdraft. The evaporation of convection precipitation is also

135   considered in this parameterization. Because the evaporation rate is associated with the deep convection precipitation flux

136   Q_{dp}, we use the ratio of the tagged deep convection precipitation flux $Q_{\mathrm{dp},tg}^k$ and the corresponding sum to calculate the

137   evaporation of tagged deep convection precipitation:

138    $$\left(\frac{\partial q_{v,tg}^k}{\partial t}\right)_{\mathrm{dp\_evap}} = \frac{Q_{\mathrm{dp},tg}^k}{\sum_{k=1}^n Q_{\mathrm{dp},tg}^k} \times \left(\frac{\partial q_v}{\partial t}\right)_{\mathrm{dp\_evap}} \tag{2}$$

139   For the temporal evolution of $q_{l,tg}^k$ and $q_{i,tg}^k$ in the deep convection parameterization, both are treated in the same

140   subroutine as q_l and q_i.

141

2.2 Shallow convection

143   The shallow convection scheme in CAM5.1 is taken from Park and Bretherton (2009). In this scheme, because the

144   detrainment of cloud water and ice ($D(q_l)$ and $D(q_i)$) is assumed to be proportional to the total water detrainment and the

Geoscientific
Model Development
Discussions

145   detrained air is assumed to be a representative of cumulus updraft (Park and Bretherton, 2009), we use the ratio of tagged

146   total water in the updraft $q_{t,u,tg}^k$ and the corresponding sum to distribute the detrainment of tagged cloud water and ice

147   ($D\left(q_{l,tg}^k\right)$ and $D\left(q_{i,tg}^k\right)$):

148   $D\left(q_{l,tg}^k\right) = \left(\frac{q_{t,u,tg}^k}{\sum_{k=1}^n q_{t,u,tg}^k}\right) \times D(q_l), \; D\left(q_{l,tg}^k\right) = (\frac{q_{t,u,tg}^k}{\sum_{k=1}^n q_{t,u,tg}^k}) \times D(q_l)$ (3)

149   This ratio is also applied to the calculations of in-cumulus tagged condensates and the production rates of tagged rain/snow

150   by cumulus expulsion of condensates to the environment. Like CAM5.1's deep convection scheme, the shallow convection

151   scheme relates precipitation evaporation rate $\left(\frac{\partial q_v}{\partial t}\right)_{\text{sh\_evap}}$ to shallow convection precipitation flux Q_{sh}. Therefore, we use an

152   assumed expression such as Eq. (2) to calculate the tagged precipitation evaporation rate:

153   $\left(\frac{\partial q_{v,tg}^k}{\partial t}\right)_{\text{sh\_evap}} = \frac{Q_{\text{sh},tg}^k}{\sum_{k=1}^n Q_{\text{sh},tg}^k} \times \left(\frac{\partial q_v}{\partial t}\right)_{\text{sh\_evap}}$ (4)

154   Tagged condensate tendencies for compensating subsidence or upwelling and penetrative entrainment mass flux are

155   calculated with the same equations as the original water-related quantities in this scheme.

156

157   **2.3 Cloud Macrophysics**

158   Park et al. (2014) provided a detailed description of CAM5.1's cloud macrophysics, in which cloud fractions, horizontal and

159   vertical overlapping structures of clouds, and net condensation rates of water vapour into cloud droplets and ice are

160   computed. Because the tendencies of water substances caused by cumulus convection have been calculated in deep and

161   shallow convection schemes, we focus on the treatment of the tagged stratus fraction and net condensation rates of tagged

162   water vapour in stratus clouds in this section.

163

164   The liquid stratus fraction $A_{l,\text{st}}$ is a unique function of grid-mean relative humidity (RH) over water, $\overline{u}_l \equiv \overline{q_v}/\overline{q_{s,w}}$, where $\overline{q_v}$

165   is the grid-mean water vapour specific humidity and $\overline{q_{s,w}}$ is the grid-mean saturation specific humidity over water, which is

166 shown in Eq. (3) of Park et al. (2014). We allocate the tagged liquid stratus fraction $A_{l,\mathrm{st},tg}^{k}$, which depends on the ratio of

167 grid-mean tagged water vapour specific humidity $\overline{q_{v,tg}^{k}}$ and the corresponding sum, expressed as:

168 $$A_{l,\mathrm{st},tg}^{k} = \frac{\overline{q_{v,tg}^{k}}}{\Sigma_{k=1}^{n} \overline{q_{v,tg}^{k}}} \times A_{l,\mathrm{st}} \tag{5}$$

169 This ratio is also used in the computation of tagged in-stratus liquid water content (LWC) $q_{l,\mathrm{st},tg}^{k}$ and tagged grid-mean

170 ambient LWC $\overline{q_{l,\mathrm{a},tg}^{k}}$, thus

171 $$q_{l,\mathrm{st},tg}^{k} = \frac{\overline{q_{v,tg}^{k}}}{\Sigma_{k=1}^{n} \overline{q_{v,tg}^{k}}} \times q_{l,\mathrm{st}} \tag{6}$$

172 and

173 $$\overline{q_{l,\mathrm{a},tg}^{k}} = \frac{\overline{q_{v,tg}^{k}}}{\Sigma_{k=1}^{n} \overline{q_{v,tg}^{k}}} \times \overline{q_{l,\mathrm{a}}} \tag{7}$$

174 Here, $q_{l,\mathrm{st}}$ is the in-stratus LWC and $\overline{q_{l,\mathrm{a}}}$ is the grid-mean ambient LWC. Similar to $A_{l,\mathrm{st}}$, the ice stratus fraction $A_{i,\mathrm{st}}$ is a

175 function of the grid-mean total ice RH over ice, $\overline{v_{\iota}} \equiv (\overline{q_{v}} + \overline{q_{\iota}})/\overline{q_{s,\iota}}$, where $\overline{q_{\iota}}$ is the grid-mean ice specific humidity and $\overline{q_{s,\iota}}$

176 is the grid-mean saturation specific humidity over ice, as shown in Eq. (4) of Park et al. (2014). Therefore, the tagged ice

177 stratus fraction $A_{i,\mathrm{st},tg}^{k}$, tagged in-stratus ice water content (IWC) $q_{i,\mathrm{st},tg}^{k}$ and subsequent tagged grid-mean ambient IWC

178 $\overline{q_{\iota,\mathrm{a},tg}^{k}}$ are all calculated based on the ratio of grid-mean total tagged ice specific humidity $(\overline{q_{v,tg}^{k}} + \overline{q_{\iota,tg}^{k}})$ and the

179 corresponding sum, expressed as:

180 $$A_{i,\mathrm{st},tg}^{k} = \frac{(\overline{q_{v,tg}^{k}} + \overline{q_{\iota,tg}^{k}})}{\Sigma_{k=1}^{n}(\overline{q_{v,tg}^{k}} + \overline{q_{\iota,tg}^{k}})} \times A_{i,\mathrm{st}} \tag{8}$$

181 $$q_{i,\mathrm{st},tg}^{k} = \frac{(\overline{q_{v,tg}^{k}} + \overline{q_{\iota,tg}^{k}})}{\Sigma_{k=1}^{n}(\overline{q_{v,tg}^{k}} + \overline{q_{\iota,tg}^{k}})} \times q_{i,\mathrm{st}} \tag{9}$$

182 $$\overline{q_{\iota,\mathrm{a},tg}^{k}} = \frac{(\overline{q_{v,tg}^{k}} + \overline{q_{\iota,tg}^{k}})}{\Sigma_{k=1}^{n}(\overline{q_{v,tg}^{k}} + \overline{q_{\iota,tg}^{k}})} \times \overline{q_{\iota,\mathrm{a}}} \tag{10}$$

183 Here, $q_{i,\mathrm{st}}$ is the in-stratus IWC and $\overline{q_{\iota,\mathrm{a}}}$ is the grid-mean ambient IWC. Using the same formula as for the calculation of the

184 grid-mean ambient water vapour specific humidity, the tagged grid-mean ambient water vapour specific humidity $\overline{q_{v,\mathrm{a},tg}^{k}}$ is

185 computed as follows:

186 $$\overline{q_{v,\text{a},tg}^{k}} = \overline{q_{v,tg}^{k}} + \overline{q_{l,tg}^{k}} + \overline{q_{i,tg}^{k}} - \overline{q_{l,\text{a},tg}^{k}} - \overline{q_{i,\text{a},tg}^{k}}$$ (11)

187

188 **2.4 Cloud Microphysics**

189 The CAM5.1 model uses the double-moment cloud microphysical scheme described in Morrison and Gettleman (2008) and

190 a modified treatment of ice supersaturation and ice nucleation from Gettleman et al. (2010). In addition, CAM5.1's stratus

191 microphysics is formulated using a single-phase stratus fraction A_{st}, which is assumed as the maximum overlap between

192 $A_{l,\text{st}}$ and $A_{i,\text{st}}$ (Park et al., 2014). In this study, the same assumption is applied to each tagged single-phase stratus fraction

193 $A_{\text{st},tg}^{k}$. The microphysical processes in CAM5.1 include condensation/deposition, evaporation/sublimation, autoconversion of

194 cloud droplets and ice to form rain and snow, accretion of cloud droplets and ice by rain or by snow, heterogeneous freezing,

195 homogeneous freezing, melting, sedimentation, activation of cloud droplets and primary ice nucleation. Detailed

196 formulations for these microphysical processes are described in Morrison and Gettleman (2008). For processes such as

197 condensation/deposition of cloud water and ice, evaporation/sublimation of cloud water and ice, conversion of cloud water to

198 rain, conversion of cloud ice to snow, accretion of cloud water and ice, freezing of cloud water and ice and ice nucleation,

199 the calculations of the tendencies of water substances can be regarded as terms multiplied by the stratus fraction. Therefore,

200 the corresponding tendencies of tagged water substances are computed by multiplication by the tagged stratus fraction, while

201 the remaining terms in the formulations remain unchanged. For calculations of melting of cloud ice and snow,

202 evaporation/sublimation of precipitation and sedimentation of cloud water and ice, the tendencies of tagged water substances

203 are computed using the same equations as for the original water substances but tagged variables are substituted for the

204 original variables of the water substances. For the calculation of the tendency of activated cloud condensation nuclei, we

205 assume that the ratio of the tendency of the tagged cloud droplets and the tendency of the original cloud droplets is equal to

206 the ratio of $A_{l,\text{st},tg}^{k}$ and the corresponding sum $\sum_{k=1}^{n} A_{l,\text{st},tg}^{k}$.

207

Geoscientific
Model Development
Discussions

EGU

Open Access

208 2.5 Advection

209 The finite volume dynamical core is chosen in this study due to its excellent properties for tracer transport (Rasch et al.,

210 2006). The CAM5.1 model can be driven by offline meteorological fields (Lamarque et al., 2012) following the procedure

211 initially developed for the Model of Atmospheric Transport and Chemistry (MARCH) (Rasch et al., 1997). In this study, the

212 external meteorological fields are obtained from Modern Era Retrospective-analysis for Research and Applications

213 (MERRA) datasets (Rienecker et al., 2011), whose horizontal resolution is identical to CAM5.1's. Temporal evolutions of

214 $q_{v,tg}^k$, $q_{l,tg}^k$ and $q_{i,tg}^k$ in the advective process are treated in the same manner as other constituents without any modification.

215

216 2.6 Vertical diffusion

217 CAM5.1's moist turbulence scheme is taken from the scheme presented by Bretherton and Park (2009), which calculates the

218 vertical transport of heat, moisture, horizontal momentum and tracers by symmetric turbulences. The vertical diffusion of

219 tagged water substances is treated by the procedure in the same way as other constituents without any modification.

220

221 2.7 Adjustment

222 Ideally, the differences between the MMRs of water substances and the sum MMRs of all corresponding tagged water

223 substances should be zero. However, there are exceptional differences in a few grid points (see supplementary Fig. S6). In

224 the supplement, Figs. S1–S5 show comparisons between the tendencies of the original water substances and the sum of the

225 tendencies of the tagged water substances for the relevant physical processes described in Sects. 2.1 through 2.6. Although

226 differences are small for most grid points, some abnormal values still appear randomly. For tagged water vapour, evident

227 biases mainly occur in cloud processes (cloud macrophysics and microphysics) and advection; for tagged cloud droplets, the

228 apparent biases generally occur in cloud processes in the tropics; for tagged cloud ice, the main differences occur in cloud

229 processes, advection and vertical diffusion. Nonlinearities in the calculations of the tendencies of water substances in the

230 physical schemes cause these differences. To reduce these accumulated biases in the relevant physical schemes, additional

231 criteria are applied to the relevant quantities of the tagged water substances:

232 (1) If the positive or negative sign of the tendency of a tagged water substance is identical to the sign of the tendency of the

233   original water substance, the absolute value of the tendency of the tagged water substance should not be larger than that

234   of the original water substance. If their signs are different, the tendency of the tagged water substance is set to zero.

235 (2) The sum of the tendencies of all tagged water substances should be equal to the tendency of the corresponding original

236   water substance in each scheme.

237

238 **3. Results and discussion**

239 **3.1 Model assessment**

240 Numaguti (1999) pointed out that the results of the tagged AWTs method suffer from the bias of the model used. Therefore,

241 we first estimate the precipitation simulated by the offline version of CAM5.1, which is compared with the Global

242 Precipitation Climatology Project (GPCP) version 2.2 combined precipitation data set (Huffman and Bolvin, 2011), as

243 shown in Fig. 2. In winter (December, January and February), high-precipitation zones are located in the tropics of the

244 Southern Hemisphere and in the mid-latitude areas of the NWP. Precipitation is generally less than 3 mm d^{-1} over most parts

245 of Eurasia. In summer (June, July and August), there is heavy precipitation over the southern and southeastern parts of

246 Eurasia and over central Africa. Although CAM5.1 generally shows a bias toward relatively high precipitation in the tropics

247 of the summer hemisphere, the precipitation pattern and amount over Eurasia and its adjacent areas is captured well by

248 CAM5.1.

249

3.2 Terrestrial and oceanic contributions to precipitation over Eurasia

250

251   Figure 3 shows the spatial distribution of the relative contribution of evaporation from all land source regions to precipitation

252   (colours). In winter, evaporation from land source regions generally contributes ~30–60% to the precipitation over Eurasia.

253   The largest contribution (~80%) is located in central China. In summer, ≥60% of precipitation over most parts of Eurasia is

254   supplied by evaporation from land, especially for the inland region where ≥80% of precipitation originates from the land

255   surface. However, the contribution of evaporation from land to summer precipitation over IND, ICP and east China is

256   generally less than 50%, due to moisture transport by the Indian summer monsoon and EASM. Overall, the contribution of

257   evaporation from land to precipitation over Eurasia is smaller in winter and larger in summer, which is consistent with the

258   variation of evaporation from the land surface over Eurasia in winter and summer as shown in Fig. 4. The pattern of

259   precipitation contributed by land evaporation is similar to that shown in Numaguti (1999). Our result is close to that of

260   Numaguti (1999) for summer but the contribution of land evaporation to precipitation is evidently larger for winter.

261

262   The distributions of the relative contributions of evaporation from the NAO, the extended north Indian Ocean (includes NIO,

263   BOB and AS) and the extended Northwest Pacific (includes NWP and SCS), which are three important moisture source

264   regions, are shown in Fig. 5. In winter, ~10–60% of the precipitation over the northern part of Eurasia originates from the

265   NAO, with a westward or northwestward increasing gradient in the relative contribution. The extended north Indian Ocean

266   supplies moisture for ~10–30% of the precipitation over the North Africa and South Asia. The extended Northwest Pacific

267   only provides moisture for 10–30% of the precipitation over the southern and eastern coastal regions of Asia. In summer,

268   evaporation from the NAO only affects precipitation over Europe, with a contribution of 10–30% to total precipitation.

269   Precipitation areas influenced by the extended north Indian Ocean extend to EA, while areas impacted by the extended

270   Northwest Pacific retreat eastward.

271

272   The arrow streamlines in Fig. 3 show the total tropospheric water vapour flux in winter and summer. There is a westward

273   component of water vapour flux over the tropics of both the extended north Indian Ocean and the extended Northwest

274   Pacific in the Northern Hemisphere in winter. In summer, there is a very large northwestward water vapour flux over the

275   NIO, turning northeastward over the BOB and AS. Over the extended Northwest Pacific, there is a northward component of

276   water vapour flux at 30°–60°N and a westward flux in the tropics between 120°E and 180°E. In addition, Fig. 4 shows strong

277   surface evaporation over the NWP and NAO in winter, while evaporation is weaker in summer. In contrast, evaporation over

278   the NIO is larger in summer and smaller in winter. These results help to explain the variations in the contributions of the

279   NAO, extended north Indian Ocean and extended Northwest Pacific to precipitation in winter and summer as shown in Fig. 5.

280

281   The overall contributions from these three oceanic regions are generally less than those in Numaguti (1999). The resolution

282   of the climate model used in Numaguti (1999) is ~5.6°, both in latitudinal and longitudinal direction. The different model

283   resolutions are a probable reason for the different quantitative contributions in our study and that of Numaguti (1999). In

284   addition, CAM5.1 is driven by MERRA data, so its surface evaporation flux is approximate to that of MERRA. MERRA

285   land evaporation is larger over South and East Asia and Northern Europe compared to other global estimates (Jiménez et al.,

286   2011), and Bosilovich et al. (2011) suggested that MERRA ocean evaporation is lower compared to other reanalyses but is

287   much closer to observation. Therefore, the bias in MERRA surface evaporation may lead to the higher land contribution and

288   lower oceanic contribution to precipitation.

289

290   **3.3 Atmospheric moisture source attribution of precipitation and water vapour over the YRV**

291   Figures 6a and 6b show the time series of evaporative contribution of each source region to precipitation over the YRV. The

292   contributions of evaporation to precipitation from the BOB and AS are lower during autumn–winter and higher during

293   spring–summer with relative contributions of ≤3.6%. Chow et al. (2008) (see their Fig. 20a) also found that evaporation from

294   the AS had little impact on precipitation over China. Supplementary Figs. S7–S10 show the distributions of 25 tagged water

295   vapour tracers and 25 tagged precipitations over Eurasia and surrounding areas in winter and summer. Figs. S7a and S9a

296   show that evaporation from the BOB contributes to water vapour and precipitation over the extended north Indian Ocean in

297   winter, corresponding to the direction of water flux shown in Fig. 3a. The centre of BOB-contributed precipitation (15 mg m$^-$

298   ^{2} s^{-1}) is located in the south of the TP in summer (Fig. S10a). In addition, the BOB supplies moisture to areas around the

Geoscientific
Model Development
Discussions

299 northeastern BOB in summer (Fig. S8a). The contribution of the SCS to precipitation is also very small (≤4.7%), which

300 supports the view of Chow et al. (2008), who suggested that the SCS may serve as a pathway for water vapour transport

301 from the southwesterly flow of the Indian summer monsoon and the easterly flow of the Northwest Pacific subtropical high.

302 A detailed discussion of this issue is presented in Sect. 3.5. The NWP serves as the dominant oceanic source region for

303 precipitation over the YRV during the whole year except during June and July. The relative contribution is ~7.7–10.1% in

304 June and July and 14.4–22.9% in other months. Evaporation from the NIO shows a clear contribution to precipitation during

305 May to October. Especially in June and July, the NIO is the dominant oceanic source region, with a contribution of ~22.5%.

306 This is in agreement with the result of a Lagrangian diagnostic method described in Baker et al. (2015) and the result of

307 sensitivity experiments in Chow et al. (2008). However, in other months, the contribution of the NIO is very small. The

308 contributions from evaporation from the BOB, AS and NIO are in phase with the EASM, which was also reported by Baker

309 et al. (2015). The ICP is an important terrestrial source region for the YRV precipitation, supplying moisture to ~9.8% of the

310 annual precipitation. The relative contribution of the ICP from April to September is close to the result of Wei et al. (2012).

311 The contribution of evaporation from the YRV to its precipitation can be regarded as the local recycling ratio, which is lower

312 (5.9–9%) in summer and higher (11–14.1%) in other seasons. In general, the contribution of evaporation from SCN is

313 comparable to the local contribution of the YRV. The relative contribution from the NEA is higher in autumn–winter and

314 lower in spring–summer, which may be associated with the shift of the EA monsoon. Though the individual contributions of

315 evaporation from the YRV or SCN are smaller than those from the NIO in summer, their combined contributions exceed

316 10%. This implies that evaporation from these two regions is important for precipitation over China. This is contrary to the

317 view expressed in Simmonds et al. (1999) and Qian et al. (2004), but consistent with Wei et al. (2012). Figures 6c and 6d

318 show a time series of evaporative contribution from each source region to the tropospheric water vapour amount over the

319 YRV. The overall relative contribution from each source region to the total water vapour amount is similar to the

320 corresponding relative contribution to precipitation shown in Figs. 6a and 6b.

321

3.4 Atmospheric moisture source attribution of precipitation and water vapour over SCN

Figures 7a and 7b show the contribution of each source region to precipitation over SCN. The NIO is the dominant source region in summer, while the NWP dominates precipitation over SCN during other seasons, which is similar to the situation over the YRV. The contribution from the NIO is 21.5–28.1% in summer. The contribution from the NWP is 8.2–15.7% in summer and ~20–33.4% during other seasons. During spring and summer, ~2.2–4% of precipitation is supplied from the BOB, with smaller contributions during other seasons. The contribution from the AS is similar to that of the BOB. In summer, only 3–4.2% of precipitation originates from the SCS, but the area contributes ~7–7.3% to the precipitation in early spring (March to April). Like precipitation over the YRV, the dominant terrestrial source region for SCN is the ICP, which contributes ~9.9% to the precipitation. In addition, ~5.7% of summer precipitation originates from SEA. Compared to precipitation over the YRV, the contribution from the TP is smaller. In addition, the contribution from the YRV is small in summer. The local recycling ratio or percentage contribution of evaporation from SCN is generally 5.5–8.8% during May to September, but larger than 10% during the remaining months. As shown in Fig. 7d, the overall relative contribution of each source region to the water vapour amount is similar to each region's contribution to precipitation over SCN.

3.5 Atmospheric moisture source attribution of water vapour over the SCS

Simmonds et al. (1999) and Lau et al. (2002) suggested that interannual variation of summer precipitation over China is associated with water vapour transport over the SCS. However, Chow et al. (2008) suggested that the SCS may act as a water vapour transport pathway where the southwesterly stream of the Indian summer monsoon and the easterly stream of the southeastern Asian monsoon meet. Previous studies have conducted sensitivity experiments or analysed the water vapour budget to indirectly determine moisture sources for the SCS. In contrast, our AWT method can directly quantify the contribution of each source region to the water vapour amount over the SCS, which is shown in Fig. 8. The local contribution of the SCS is small (~5–5.8%) in summer, and the mean contribution in other months is ~7.4%. The contribution of the NIO shows clear seasonal variations: the contribution is high during May to October, but very small during the other months. Similar to the results for water vapour over the YRV and SCN, the NIO is the dominant source

346 region from June to September, with a contribution of 20.8–26.9%. During this period, the contribution of the NWP is 13.3–

347 19%. However, the NWP dominates the water vapour over the SCS in the remaining months, with contributions of 23.8–

348 45.1%. In addition, the SP and NEP are also important oceanic source regions, with combined annual contributions of ~13–

349 17.7%. The most important terrestrial moisture source region is the SEA, whose contribution is larger (13.7–16.1%) in

350 summer and smaller (~6.4%) in winter. During late autumn to winter, about 5.2–6.2% of water vapour is supplied from NEA,

351 but its contribution is very small in other seasons. The other land source regions contribute relatively little to the water

352 vapour amount over the SCS.

353

354 From the SCS to SCN and further to the YRV (from south to north), surface evaporation from the SCS generally represents a

355 small (≤5.8%) contribution to the water vapour amount over the three target areas in summer. In contrast, much more water

356 vapour is supplied by evaporation from the NWP and NIO. This confirms the inference proposed by Chow et al. (2008) that

357 the SCS is a water vapour transport pathway where moisture from the NIO and NWP meet in summer.

358

359 **4. Conclusions**

360 In this study, an Eulerian tagged AWT method was implemented in CAM5.1, which provides the capacity to separately trace

361 the behaviour of atmospheric water substances originating from various moisture source regions and to quantify their

362 contributions to atmospheric water over an arbitrary region. Numaguti (1999) pointed out that the weakness of the tagged

363 AWT method is that its results suffer from the performance of the model in reproducing the hydrological cycle. However, a

364 comparison between GPCP and CAM5.1 precipitation shows that CAM5.1 has the capability to represent precipitation

365 processes. Using this method, we investigated the contribution of evaporation from land, as well as the contributions from

366 the NAO, extended north Indian Ocean and extended Northwest Pacific to precipitation over Eurasia. Our results are similar

367 to those of Numaguti (1999), except that our results indicate a larger contribution from terrestrial source regions, while the

368 three oceanic regions show smaller contributions. Different model resolutions and a bias in MERRA surface evaporation are

369 probable causes for the differences between our results and those of Numaguti (1999).

370

371   We then investigated the contribution of various source regions to precipitation and water vapour amounts over the YRV and

372   SCN. Our results suggest that the dominant oceanic moisture source region during summer is the NIO (15.9–22.5% of

373   precipitation over the YRV; 21.5–28.1% of precipitation over SCN), consistent with Baker et al. (2015) and Chow et al.

374   (2008), while during other seasons, the NWP is the dominant source region (14.3–22.9% of precipitation over the YRV;

375   14.4–34.1% of precipitation over SCN), with smaller contributions from the BOB, AS and SCS. The ICP is an important

376   terrestrial source region, with a mean annual contribution of ~10%. For precipitation over the YRV, the combined

377   contribution of evaporation from the YRV and SCN is non-negligible (exceeding 10%), consistent with Wei et al. (2012).

378   For precipitation over SCN, the local recycling ratio is generally 5.5–8.8% during May to September, and reaches 11.1–19.6%

379   in other months. The contribution from the YRV is very small in summer. The overall relative contribution of each source

380   region to the water vapour amount is similar to the corresponding contribution to precipitation over the YRV and SCN.

381

382   An analysis of water vapour amount over the SCS shows that the NIO is the dominant source region (20.8–26.9% of water

383   vapour) during June to September, while the NWP dominates (23.8–45.1% of water vapour) in the remaining months. In

384   contrast, the local contribution of the SCS is smaller (~5–5.8%) in summer. In addition, the SP, NEP and SEA are also

385   important source regions. Evaporation over the SCS represents a small contribution to water vapour amounts over the SCS,

386   SCN and the YRV in summer, implying that the SCS acts as a water vapour transport pathway rather than a dominant source

387   region, which confirms the inference of Chow et al. (2008).

388

389   At present, the tagged AWT method has only been applied to a few GCMs and regional models, and has generally focused

390   on identifying the moisture distribution over few regions such as NAM (Bosilovich and Schubert, 2002; Bosilovich et al.,

391   2003). We expect that the AWT method will be applied to additional models and used to identify moisture sources over

392   more climate regions, which will improve our understanding of atmospheric moisture transport.

393

Geoscientific Model Development Discussions

EGU Open Access

394 **Code availability**

395 The source code modifications for CAM5.1 are available from the authors. Interested readers should contact us via

396 arthur_pc@163.com or binzhu@nuist.edu.cn.

397

402

403 **References**

404 Baker, A. J., Sodemann, H., Baldini, J. U. L., Breitenbach, S. F. M., Johnson, K. R., van Hunen, J., and Zhang, P.:

405   Seasonality of westerly moisture transport in the East Asian summer monsoon and its implications for interpreting

406   precipitation δ^{18}O, J. Geophys. Res. Atmos., 120(12), 5850–5862, doi:10.1002/2014JD022919, 2015.

407 Bosilovich, M. G.: On the vertical distribution of local and remote sources of water for precipitation, Meteorol. Atmos. Phys.,

408   80(1), 31–41, doi:10.1007/s007030200012, 2002.

409 Bosilovich, M. G. and Schubert, S. D.: Water vapor tracers as diagnostics of the regional hydrologic cycle, J.

410   Hydrometeorol., 3(2), 149–165, doi:http://dx.doi.org/10.1175/1525-7541(2002)003<0149:WVTADO>2.0.CO;2, 2002.

411 Bosilovich, M. G., Robertson, F. R., Chen, J.: Global energy and water budgets in MERRA, J. Climate, 24(22), 5721–5739,

412   doi:http://dx.doi.org/10.1175/2011JCLI4175.1, 2011.

413 Bosilovich, M. G., Sud, Y. C., Schubert, S. D., and Walker, G. K.: Numerical simulation of the large-scale North American

414   monsoon water sources, J. Geophys. Res. Atmos., 108(D16), 8614, doi:10.1029/2002JD003095, 2003.

415   Bretherton, C. S. and Park, S.: A new moist turbulence parameterization in the Community Atmosphere Model, J. Climate,

416   22(12), 3422–3448, doi:http://dx.doi.org/10.1175/2008JCLI2556.1, 2009.

417   Brubaker, K. L., Entekhabi, D., and Eagleson, P. S.: Estimation of continental precipitation recycling, J. Clim., 6(6), 1077–

418   1089, doi:http://dx.doi.org/10.1175/1520-0442(1993)006<1077:EOCPR>2.0.CO;2, 1993.

419   Burde, G. I. and Zangvil, A.: The estimation of regional precipitation recycling. Part I: Review of recycling models, J. Clim.,

420   14(12), 2497–2508, doi:http://dx.doi.org/10.1175/1520-0442(2001)014<2497:TEORPR>2.0.CO;2, 2001.

421   Chen, B., Xu, X. D., and Zhao, T.: Main moisture sources affecting lower Yangtze River Basin in boreal summers during

422   2004–2009, Int. J. Climatol., 33(4), 1035–1046, doi:10.1002/joc.3495, 2013.

423   Chow, K. C., Tong, H. W., and Chan, J. C.: Water vapor sources associated with the early summer precipitation over China,

424   Clim. Dynam., 30(5), 497–517, doi:10.1007/s00382-007-0301-6, 2008.

425   Dirmeyer, P. A. and Brubaker, K. L.: Contrasting evaporative moisture sources during the drought of 1988 and the flood of

426   1993, J. Geophys. Res., 104(D16), 19383–19397, doi:10.1029/1999JD900222, 1999.

427   Drumond, A., Nieto, R., and Gimeno, L.: Sources of moisture for China and their variations during drier and wetter

428   conditions in 2000−2004: a Lagrangian approach, Clim. Res., 5, 215–225, doi:10.3354/cr01043, 2011.

429   Eltahir, E. A. and Bras, R. L.: Precipitation recycling, Rev. Geophys., 34(3), 367–378, doi:10.1029/96RG01927, 1996.

430   Emmons, L. K., Walters, S., Hess, P. G., Lamarque, J.-F., Pfister, G. G., Fillmore, D., Granier, C., Guenther, A., Kinnison,

431   D., Laepple, T., Orlando, J., Tie, X., Tyndall, G., Wiedinmyer, C., Baughcum, S. L., and Kloster, S.: Description and

432   evaluation of the Model for Ozone and Related chemical Tracers, version 4 (MOZART-4), Geosci. Model Dev., 3(1),

433   43–67, doi:10.5194/gmd-3-43-2010, 2010.

434   Gettelman, A., Liu, X., Ghan, S. J., Morrison, H., Park, S., Conley, A. J., Klein, S. A., Boyle, J., Mitchell, D. L., and Li, J.-L.

435   F.: Global simulations of ice nucleation and ice supersaturation with an improved cloud scheme in the Community

436   Atmosphere Model, J. Geophys. Res., 115, D18216, doi:10.1029/2009JD013797, 2010.

437   Gimeno, L., Stohl, A., Trigo, R. M., Dominguez, F., Yoshimura, K., Yu, L., Drumond, A., Durán-Quesada, A. M., and Nieto,

438   R.: Oceanic and terrestrial sources of continental precipitation, Rev. Geophys., 50, RG4003,

439   doi:10.1029/2012RG000389, 2012.

440 Gustafsson, M., Rayner, D. and Chen, D.: Extreme rainfall events in southern Sweden: where does the moisture come from?

441   Tellus A, 62, 605–616, doi:10.1111/j.1600-0870.2010.00456.x, 2010.

442 Held, I. M. and Soden, B. J.: Water vapor feedback and global warming, Annu. Rev. Energy Environ., 25, 441–475,

443   doi:10.1146/annurev.energy.25.1.441, 2000.

444 Huffman, G. J. and Bolvin, D. T.: GPCP version 2.2 combined precipitation data set documentation, NASA Goddard Space

445   Flight Center, Mesoscale Atmospheric Processes Laboratory and Science Systems and Applications, Inc., 2011.

446 Jiménez, C., Prigent, C., Mueller, B., Seneviratne, S. I., McCabe, M. F., Wood, E. F., Rossow, W. B., Balsamo, G., Betts, A.

447   K., Dirmeyer, P. A., Fisher, J. B., Jung, M., Kanamitsu, M., Reichle, R. H., Reichstein, M., Rodell, M., Sheffield, J., Tu,

448   K., and Wang, K.: Global intercomparison of 12 land surface heat flux estimates, J. Geophys. Res., 116, D02102,

449   doi:10.1029/2010JD014545, 2011.

450 Joussaume, S., Sadourny, R., and Vignal, C.: Origin of precipitating water in a numerical simulation of the July climate,

451   Ocean-Air Inter., 1, 43–56, 1986.

452 Knoche, H. R. and Kunstmann, H.: Tracking atmospheric water pathways by direct evaporation tagging: A case study for

453   West Africa, J. Geophys. Res. Atmos., 118, 12345–12358, doi:10.1002/2013JD019976, 2013.

454 Koster, R., Jouzel, J., Suozzo, R., Russell, G., Broecker, W., Rind, D., and Eagleson, P.: Global sources of local precipitation

455   as determined by the NASA/GISS GCM, Geophys. Res. Lett., 13(2), 121–124, doi:10.1029/GL013i002p00121, 1986.

456 Lamarque, J.-F., Emmons, L. K., Hess, P. G., Kinnison, D. E., Tilmes, S., Vitt, F., Heald, C. L., Holland, E. A., Lauritzen, P.

457   H., Neu, J., Orlando, J. J., Rasch, P. J., and Tyndall, G. K.: CAM-chem: description and evaluation of interactive

458   atmospheric chemistry in the Community Earth System Model, Geosci. Model Dev., 5, 369–411, doi:10.5194/gmd-5-

459   369-2012, 2012.

460 Lau, K. M., Li, X., and Wu, H. T.: Evolution of the large scale circulation, cloud structure and regional water cycle

461   associated with the South China Sea monsoon during May–June, 1998, J. Meteor. Soc. Japan. Ser. II, 80(5), 1129–1147,

462   doi:10.2151/jmsj.80.1129, 2002.

463   Morrison, H. and Gettelman, A.: A new two-moment bulk stratiform cloud microphysics scheme in the Community

464   Atmosphere Model, version 3 (CAM3). Part I: Description and numerical tests, J. Climate, 21(15), 3642–3659,

465   doi:http://dx.doi.org/10.1175/2008JCLI2105.1, 2008.

466   Neale, R. B., Chen, C.-C., Gettelman, A., Lauritzen, P. H., Park, S., Williamson, D. L., Conley, A. J., Garcia, R., Kinnison,

467   D., Lamarque, J.-F., Marsh, D., Mills, M., Smith, A. K., Tilmes, S., Vitt, F., Morrison, H., Gameron-Smith, P., Collins,

468   W. D., Iacono, M. J., Easter, R. C., Ghan, S. J., Liu, X., Rasch, P. J., and Taylor, M. A.: Description of the NCAR

469   Community Atmosphere Model (CAM5), NCAR Technical Note NCAR/TN-486+STR, 275 pp, 2012.

470   Numaguti, A.: Origin and recycling processes of precipitating water over the Eurasian continent: Experiments using an

471   atmospheric general circulation model, J. Geophys. Res., 104(D2), 1957–1972, doi:10.1029/1998JD200026, 1999.

472   Park, S. and Bretherton, C. S.: The University of Washington shallow convection and moist turbulence schemes and their

473   impact on climate simulations with the Community Atmosphere Model, J. Climate, 22(12), 3449–3469,

474   doi:http://dx.doi.org/10.1175/2008JCLI2557.1, 2009.

475   Park, S., Bretherton, C. S., and Rasch, P. J.: Integrating cloud processes in the Community Atmosphere Model, version 5, J.

476   Climate, 27(18), 6821–6856, doi:http://dx.doi.org/10.1175/JCLI-D-14-00087.1, 2014.

477   Qian, J. H., Tao, W. K., and Lau, K. M.: Mechanisms for Torrential Rain Associated with the Mei-Yu Development during

478   SCSMEX   1998,   Mon.   Wea.   Rev.,   132(1),   3–27,   doi:http://dx.doi.org/10.1175/1520-

479   0493(2004)132<0003:MFTRAW>2.0.CO;2, 2004.

480   Rasch, P. J., Coleman, D. B., Mahowald, N., and Williamson, D. L.: Characteristics of Atmospheric Transport Using Three

481   Numerical Formulations for Atmospheric Dynamics in a Single GCM Framework, J. Climate, 19(11), 2243–2266,

482   doi:http://dx.doi.org/10.1175/JCLI3763.1, 2006.

483   Rasch, P. J., Mahowald, N. M., and Eaton, B. E.: Representations of transport, convection, and the hydrologic cycle in

484   chemical transport models: Implications for the modeling of short-lived and soluble species, J. Geophys. Res., 102,

485   28127–28138, doi:10.1029/97JD02087, 1997.

486   Raymond, D. J. and Blyth, A. M.: A stochastic mixing model for nonprecipitating cumulus clouds, J. Atmos. Sci., 43(22),

487   2708–2718, doi:http://dx.doi.org/10.1175/1520-0469(1986)043<2708:ASMMFN>2.0.CO;2, 1986.

Geoscientific
Model Development
Discussions

488 Raymond, D. J. and Blyth, A. M.: Extension of the stochastic mixing model to cumulonimbus clouds, J. Atmos. Sci., 49(21),

489   1968–1983, doi:http://dx.doi.org/10.1175/1520-0469(1992)049<1968:EOTSMM>2.0.CO;2, 1992.

490 Richter, J. H. and Rasch, P. J.: Effects of convective momentum transport on the atmospheric circulation in the community

491   atmosphere model, version 3, J. Climate, 21(7), 1487–1499, doi:http://dx.doi.org/10.1175/2007JCLI1789.1, 2008.

492 Rienecker, M. M., Suarez, M. J., Gelaro, R., Todling, R., Bacmeister, J., Liu, E., Bosilovich, M. G., Schubert, S. D., Takacs,

493   L., Kim, G.-K., Bloom, S., Chen, J., Collins, D., Conaty, A., da Silva, A., Gu, W., Joiner, J., Koster, R. D., Lucchesi, R.,

494   Molod, A., Owens, T., Pawson, S., Pegion, P., Redder, C. R., Reichle, R., Robertson, F. R., Ruddick, A. G.,

495   Sienkiewicz, M., and Woollen, J.: MERRA: NASA's Modern-Era Retrospective analysis for Research and Applications,

496   J. Climate, 24(14), 3624–3648, doi:http://dx.doi.org/10.1175/JCLI-D-11-00015.1, 2011.

497 Savenije, H. H. G.: New definitions for moisture recycling and the relationship with land-use changes in the Sahel, J. Hydrol.,

498   167, 57–78, doi:10.1016/0022-1694(94)02632-L, 1995.

499 Simmonds, I., Bi, D. and Hope, P.: Atmospheric Water Vapor Flux and Its Association with Rainfall over China in Summer,

500   J. Climate, 12(5), 1353–1367, doi:http://dx.doi.org/10.1175/1520-0442(1999)012<1353:AWVFAI>2.0.CO;2, 1999.

501 Sodemann, H. and Zubler, E.: Seasonal and interannual variability of the moisture sources for Alpine precipitation during

502   1995–2002, Int. J. Climatol., 30, 947–961, doi:10.1002/joc.1932, 2010.

503 Sodemann, H., Schwierz, C., and Wernli, H.: Interannual variability of Greenland winter precipitation sources: Lagrangian

504   moisture diagnostic and North Atlantic Oscillation influence, J. Geophys. Res., 113, D03107,

505   doi:10.1029/2007JD008503, 2008.

506 Sodemann, H., Wernli, H. and Schwierz, C.: Sources of water vapour contributing to the Elbe flood in August 2002—A

507   tagging study in a mesoscale model, Q.J.R. Meteorol. Soc., 135, 205–223, doi:10.1002/qj.374, 2009.

508 Stohl, A. and James, P.: A Lagrangian analysis of the atmospheric branch of the global water cycle. Part I: Method

509   description, validation, and demonstration for the August 2002 flooding in central Europe, J. Hydrometeorol., 5(4),

510   656–678, doi:http://dx.doi.org/10.1175/1525-7541(2004)005<0656:ALAOTA>2.0.CO;2, 2004.

Geoscientific
Model Development
Discussions

511 Stohl, A., Forster, C., and Sodemann, H.: Remote sources of water vapor forming precipitation on the Norwegian west coast

512   at 60° N – a tale of hurricanes and an atmospheric river, J. Geophys. Res., 113, D05102, doi:10.1029/2007JD009006,

513   2008.

514 Trenberth, K. E.: Atmospheric moisture recycling: Role of advection and local evaporation, J. Clim., 12(5), 1368–1381,

515   doi:http://dx.doi.org/10.1175/1520-0442(1999)012<1368:AMRROA>2.0.CO;2, 1999.

516 Wei, J., Dirmeyer, P. A., Bosilovich, M. G., and Wu, R.: Water vapor sources for Yangtze River Valley rainfall:

517   Climatology, variability, and implications for rainfall forecasting, J. Geophys. Res. Atmos., 117, D05126,

518   doi:10.1029/2011JD016902, 2012.

519 Xu, X. D., Shi, X. Y., Wang, Y. Q., Peng, S. Q., and Shi, X. H.: Data analysis and numerical simulation of moisture source

520   and transport associated with summer precipitation in the Yangtze River Valley over China, Meteorol. Atmos. Phys.,

521   100(1), 217–231, doi:10.1007/s00703-008-0305-8, 2008.

522 Zhang, G. J. and McFarlane, N. A.: Sensitivity of climate simulations to the parameterization of cumulus convection in the

523   Canadian   Climate   Centre   general   circulation   model,   Atmos.   Ocean,   33(3),   407–446,
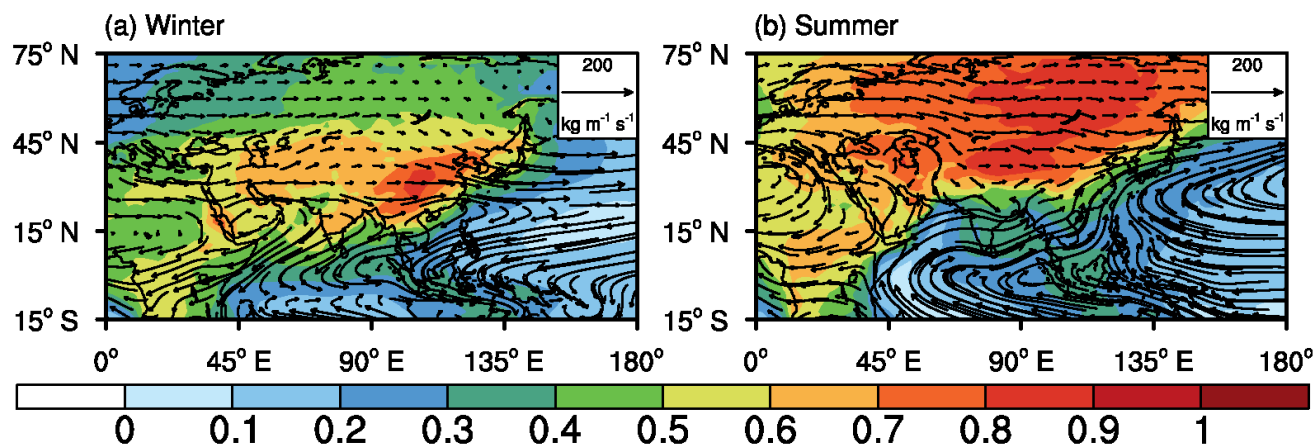
524   doi:10.1080/07055900.1995.9649539, 1995.

525

Geoscientific
Model Development
Discussions
EGU
Open Access
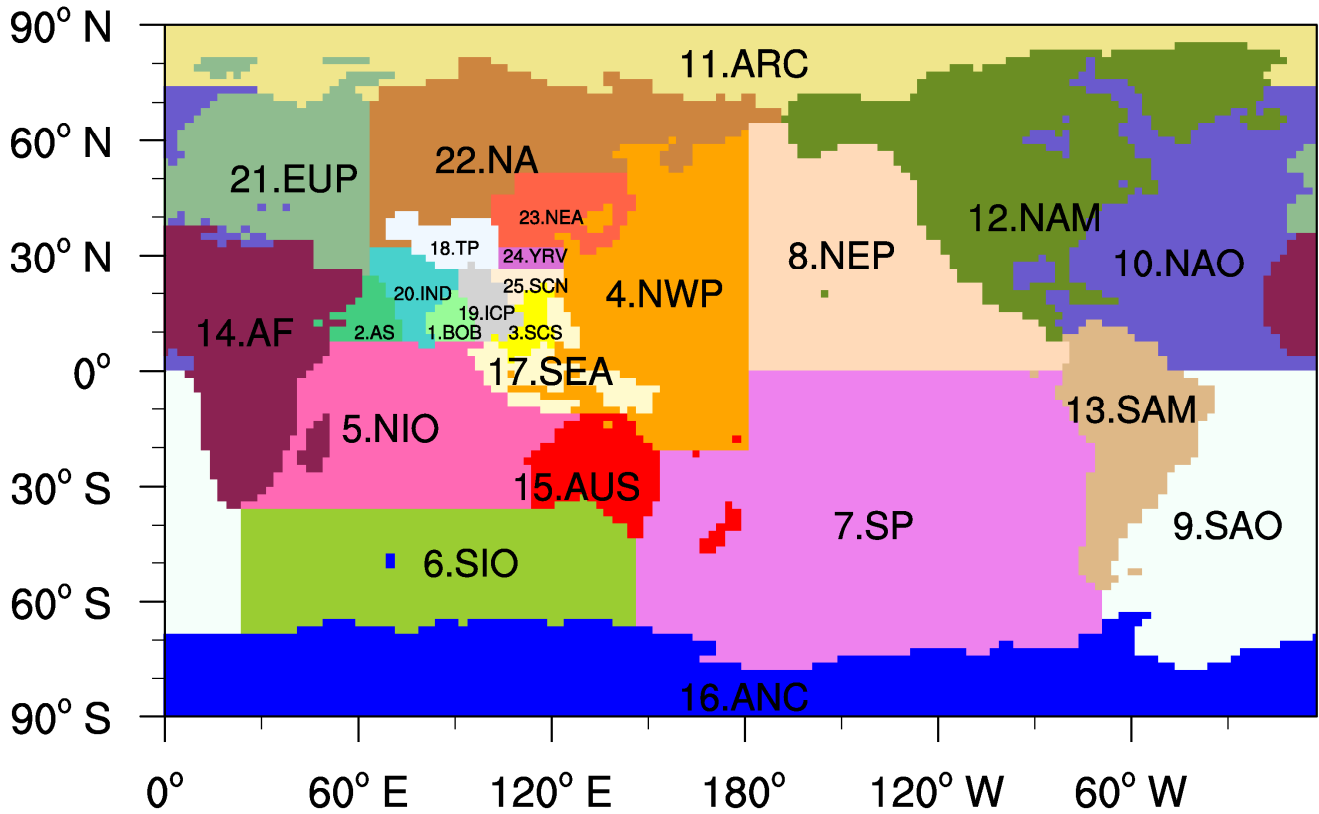
Figure 1. Moisture source regions: the regions are denoted as (1) Bay of Bengal: BOB; (2) Arabian Sea: AS; (3) South China Sea: SCS; (4) Northwest Pacific: NWP; (5) north Indian Ocean: NIO; (6) southern Indian Ocean: SIO; (7) southern Pacific: SP; (8) Northeast Pacific: NEP; (9) southern Atlantic Ocean: SAO; (10) northern Atlantic Ocean: NAO; (11) Arctic Ocean: ARC; (12) North America: NAM; (13) South America: SAM; (14) Africa: AF; (15) Australia: AUS; (16) Antarctic: ANC; (17) Southeast Asia: SEA; (18) Tibet Plateau: TP; (19) Indo-China Peninsula: ICP; (20) India: IND; (21) Europe: EUP; (22) North Asia: NA; (23) Northeast Asia: NEA; (24) Yangtze River Valley: YRV; (25) South China: SCN.
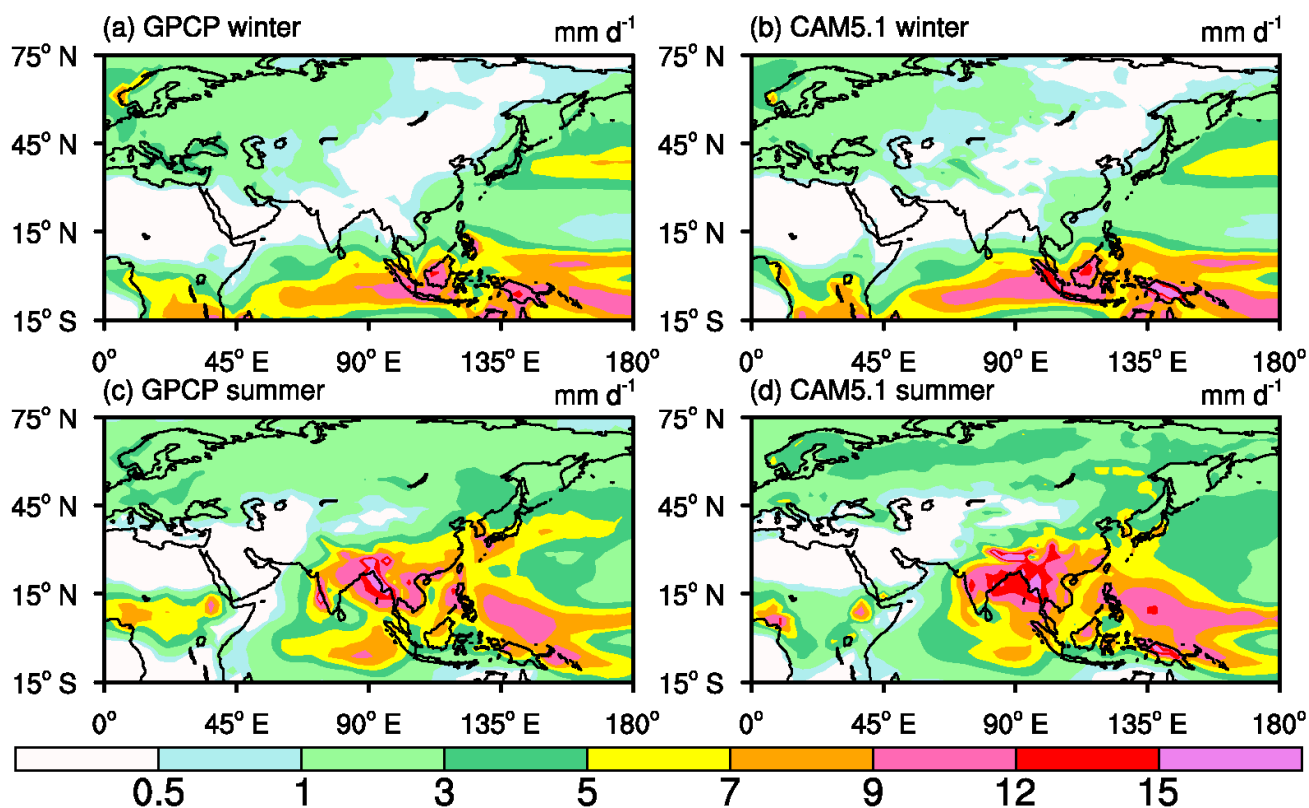
Figure 2. Comparisons between (left) GPCP data and (right) CAM5.1 precipitation simulations during (top) winter and (bottom) summer (ten-year averages for 1998 to 2007).

Figure 3. Distribution of the relative contribution to precipitation from all land source regions defined in **Fig. 1** (colours, unit: 1) and vertically integrated tropospheric water vapour flux (arrow streamlines, unit: kg m⁻¹ s⁻¹) during (a) winter and (b) summer.
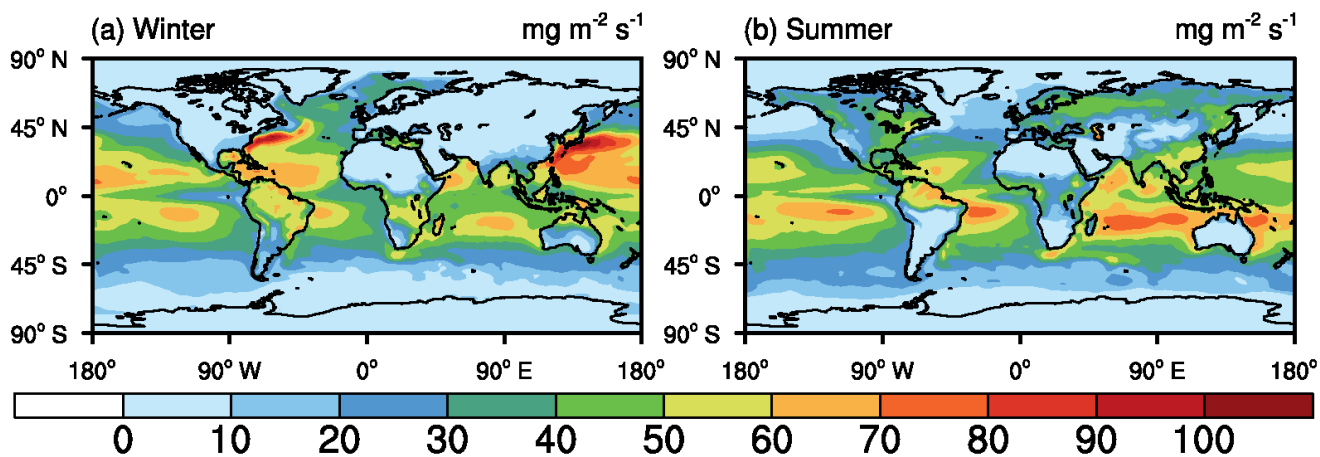
Figure 4. Distribution of CAM5.1's ten-year averaged surface evaporation flux (unit: mg m^{-2} s^{-1}) in (a) winter and (b) summer between 1998 and 2007.
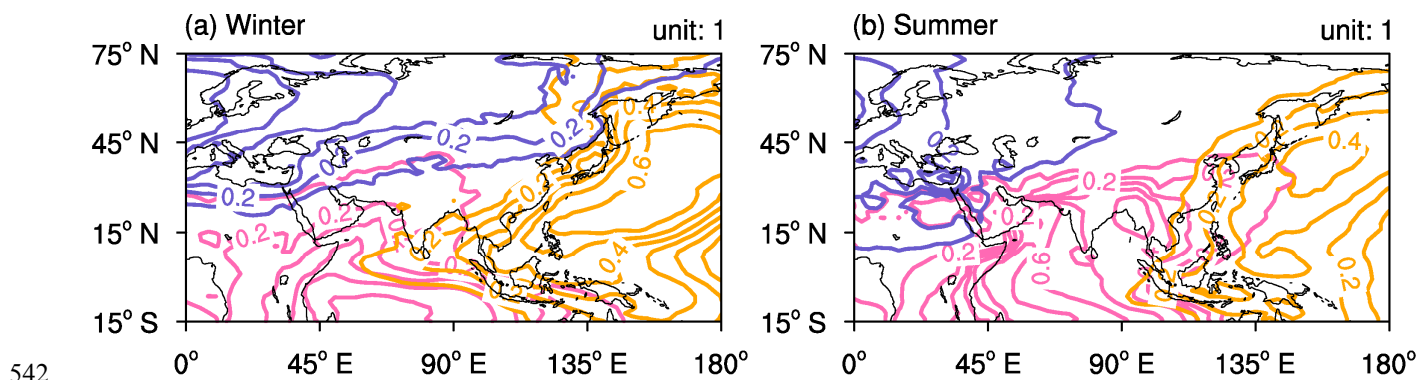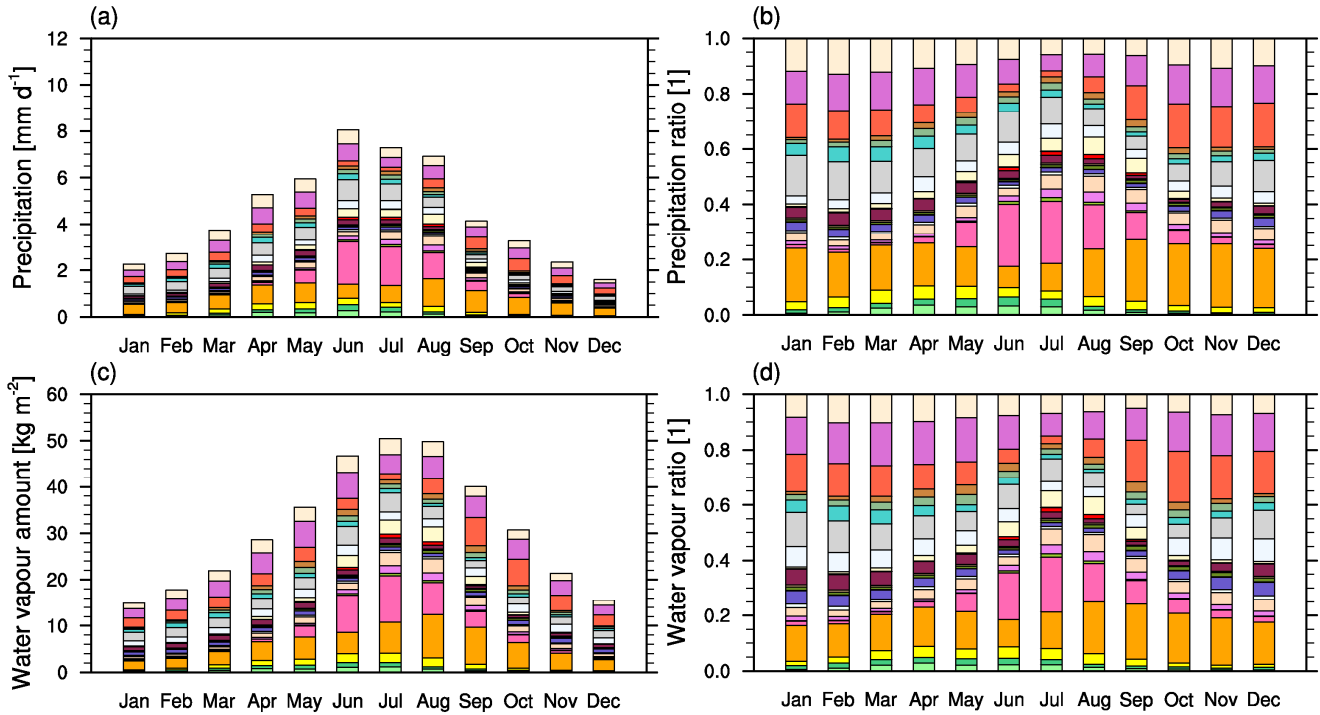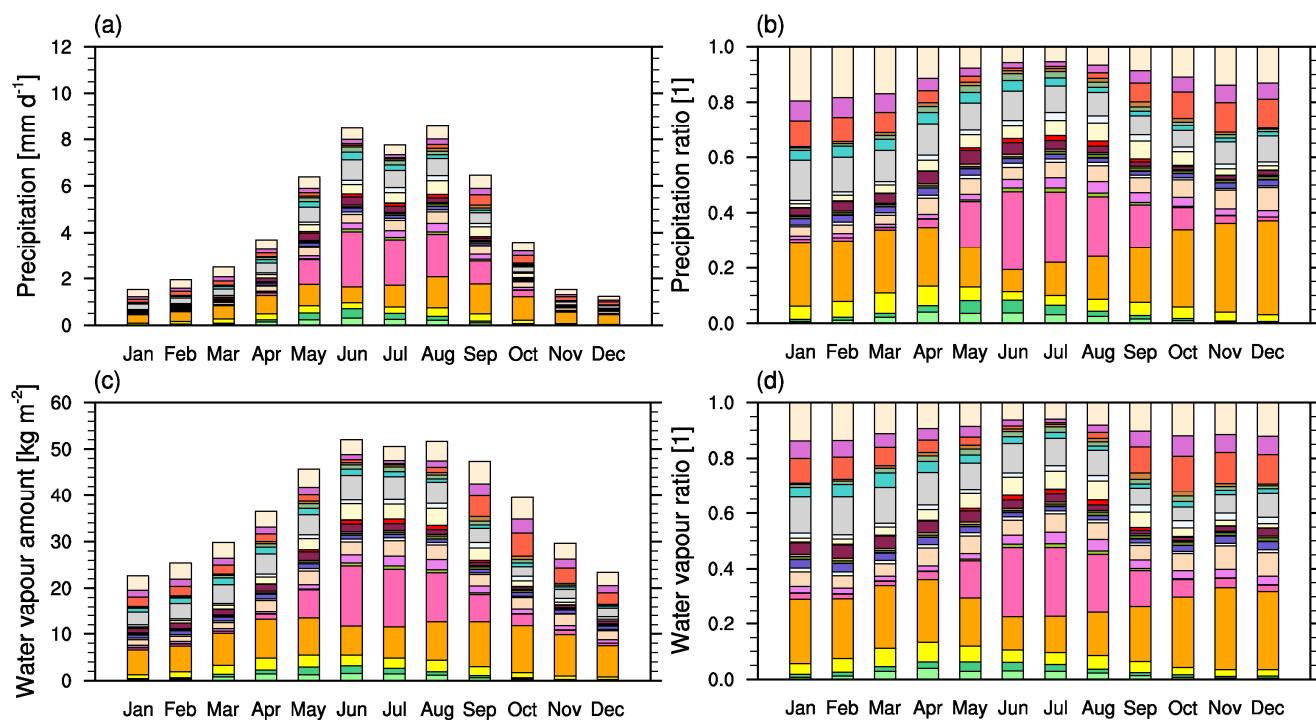
Figure 5. Distributions of the ratios of precipitation (unit: 1) supplied from the NAO (slate blue), the extended north Indian Ocean (NIO + BOB + AS, pink), and the extended Northwest Pacific (NWP + SCS, orange) during (a) winter and (b) summer. Contour interval is 0.1.
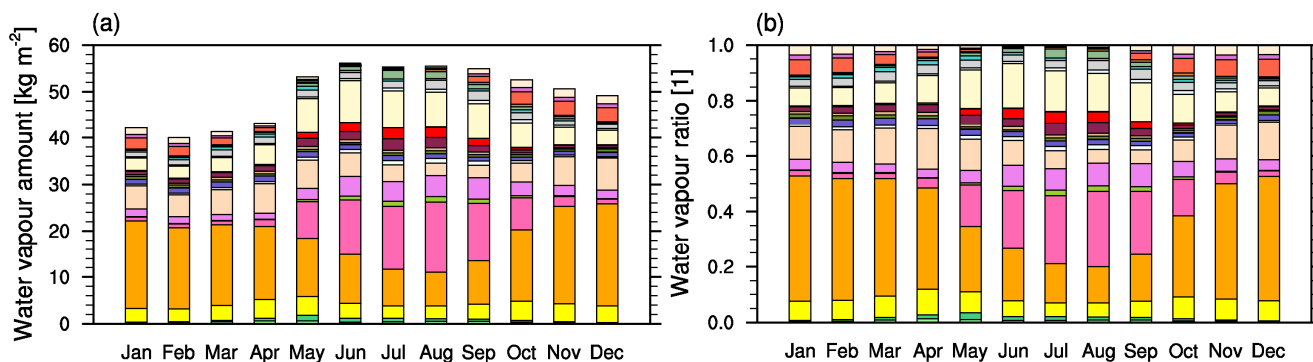
Figure 6. (a) Monthly averaged evaporative contributions of 25 defined source regions to the precipitation over the YRV. (b) Same as **Fig. 6a**, but for the relative contribution to precipitation. (c) Monthly averaged evaporative contributions of 25 defined source regions to the tropospheric total water vapour amount over the YRV. (d) Same as **Fig. 6c**, but for the relative contribution to water vapour. Stacked column colours correspond to source region colours in **Fig. 1**.

Figure 7. Same as **Fig. 6**, but for the contributions and relative contributions of 25 source regions to precipitation and tropospheric total water vapour amount over SCN.

Figure 8. (a) Monthly averaged evolution of evaporative contribution of 25 defined source regions to the tropospheric total water vapour amount over the SCS. (b) Same as **Fig. 8a**, but for the relative contribution of water vapour. Stacked column colours correspond to source region colours in **Fig. 1**.